Inverse Problems and Imaging
Vol. 17, No. 2, April 2023, pp. 490-506
doi:10.3934/ipi.2022054

SUPER-LOCALISATION OF A POINT-LIKE EMITTER IN A RESONANT ENVIRONMENT: CORRECTION OF THE MIRAGE EFFECT

Lorenzo Baldassari[1], Pierre Millien[*2] and Alice L. Vanel[3]

[1]CMOR Department, Rice University, Houston, TX 77005, USA

[2]ESPCI Paris, PSL Research University, CNRS, Institut Langevin, France

[3]CERN, 1211 Geneva 23, Switzerland

(Communicated by Habib Ammari)

Abstract. In this paper, we show that it is possible to overcome one of the fundamental limitations of super-resolution microscopy: the necessity to be in an *optically homogeneous* environment. Using recent modal approximation results from [10, 7], we show, as a proof of concept, that it is possible to recover the position of a single point-like emitter in a *known resonant environment* from far-field measurements, with a precision two orders of magnitude below the classical Rayleigh limit. The procedure does not involve solving any partial differential equation, is computationally light (optimisation in $\mathbb{R}^d$ with d of the order of 10) and is therefore suited for the recovery of a very large number of single emitters.

1. Introduction.

1.1. Context and position of the problem.

Super-resolution imaging [20, 19] has had a huge impact on biological imaging (its contribution was recognised by the Nobel Prize in 2014 [15]). The techniques introduced in [20, 19] allow details recovery for biological structures two orders of magnitude below the classical diffraction limit of microscopy. Super-resolution techniques are now being used in other areas of material science such as polymer dynamics study [17, 29] and plasmonics [11]. We refer the reader to the review paper [30] and references therein for an overview of the recent research on plasmonics using super-resolved microscopy.

Super-resolution microscopy's principle is to excite a single point-like emitter in a diffraction-limited spot, and to recover the emitter position by fitting a point-spread function over the spot. The procedure is iterated thousands of times to reconstruct a precise image, in a similar way to the technique of *pointillism* in painting. There are several types of microscopy depending on whether or not the excitation of the emitters is tailored to their emissive properties. The latter is what can be called

2020 *Mathematics Subject Classification.* Primary: 35R30, 35C20; Secondary: 65R32.

Key words and phrases. Plasmonic resonance, biomedical imaging, mirage effect, super-resolution, super-localisation.

This work was supported by the DOE under grant number [DE-SC0020345] and by the Swiss National Science Foundation under grant number [200021-172483].

*Corresponding author: Pierre Millien.

localisation-based super-resolution imaging, and is known under different acronyms such as STORM, PALM, PAINT, etc.

Single emitters such as quantum dots or fluorescent molecules interact with their environment in several ways.

The lifetime emission of single fluorescent molecules is known to depend on the local density of states (LDOS) and therefore the molecules constitute excellent candidates for probing the near-field around a nano-structure. In [11], the authors experimentally measured the lifetime of single emitters around a plasmonic rod while simultaneously super-localising the emitters. They were able to construct a map of the fluorescence lifetime with a resolution approaching 20 nm.

However, the single emitter can also excite the plasmonic resonances of the nano-structure nearby if its emission frequency is close to a plasmonic resonant frequency. In this case, the far-field image does not only consist of the point spread function of the single emitter but also contains artefacts due to the electromagnetic field scattered by the resonant nanoparticle. In [27], the coupling between the plasmonic particle and the fluorescent molecule leads to an incorrect molecular localisation of up to 30 nm, namely a single-molecule mirage. We refer to the review [30] and references therein for more details on molecular localisation shifting.

The state-of-the-art solution to this problem is to perform a least-square optimisation on the emitter position, by simulating the measurements at each step and solving the full Maxwell system with a different source position at every step. This method could give satisfying results for the localisation of one emitter, but the computational cost renders this method impossible to use to get a real super-resolution image, as the single emitter localisation procedure needs to be done thousands of times to get an image.

The challenge is therefore to find a model that is accurate enough to precisely describe the interaction between a single emitter and a resonant structure, yet computationally light enough to be able to retrieve the positions of tens of thousands of emitters.

1.2. **Mathematical challenges and recent advances.** A natural approach to tackle this problem is to model the response of the plasmonic system with excitation independant quantities. An intuitive way to do this is to use modal analysis. The idea is to express the measured field as a sum of two fields: the field generated by the single point-wise emitter and the field contributed by the nanoparticle (approximated by a few modes). The obvious strength of this description is that the modes can be pre-computed, and the procedure of solving the forward problem can be reduced to computing the modal excitation coefficients.

The main challenge is that the mirage phenomenon happens in a regime where the extinction cross section of the nanoparticle is dominated by the scattering cross section. This happens for larger nanoparticles, of typical size larger than 50 nm (see [6, section 4] for more details).

While there has been plenty of work on the mathematical description of plasmonic resonances as an eigenvalue problem [18, 8, 1], most of these works rely on an electro-static approximation that fails to characterise the behaviour of metallic nanoparticles as their size becomes *small but comparable to the wavelength* of the electromagnetic field. For instance, when the size of the nanoparticle is larger than one tenth of the wavelength (around 50 nm in practice), the quasi-static theory breaks down [21, 23]. It is only recently, via the introduction of a perturbative spectral method, that the field scattered by larger nanoparticles has been precisely

described [5, 10, 7]. In this paper, using these latest perturbed modal decompositions, we tackle the problem of super-localising a single emitter placed near a plasmonic structure in the regime that is relevant for applications.

1.3. **Contribution of the paper.** Using a simple scalar *toy model* that still encompasses all the mathematical complexity of plasmonic resonances, we show that it is possible to recover the position of a single point-like emitter near a resonant structure up to a precision that is two orders of magnitudes below the diffraction limit with a low computational complexity.

The paper is structured as follows: in section 2 we present the mathematical modelling of the physical system and justify its relevance. Then, in section 3, we derive the modal approximation of the field. In section 4, we move on to introducing the imaging functionals that allow the reconstruction of the emitter's position and orientation. Finally, we perform numerical experiments in section 5 that show the soundness and robustness of our method. We give concluding remarks in section 6.

2. Mathematical modelling of the physical system.

2.1. **Notations.** We consider a system composed of a single point-like dipole source (modelling a fluorescent molecule) and a plasmonic particle embedded in a homogeneous medium. The plasmonic particle occupies a bounded simply connected domain $D \subset \mathbb{R}^2$ of class $C^{1,\alpha}$ for some $0 < \alpha < 1$. It has a characteristic size δ. The point-like source is modelled by an ideal electric dipole of centre $z^* \in \mathbb{R}^2 \setminus \overline{D}$ and direction $\mathbf{p}^* \in \mathbb{S}^1$ [27]. We denote the permittivity of the plasmonic particle by ε_D. The permittivity of the background medium is denoted by ε_m. In other words, the permittivity distribution ε is given by

$$\varepsilon = \varepsilon_D \chi(D) + \varepsilon_m \chi\left(\mathbb{R}^2 \setminus \overline{D}\right).$$

Note that ε_D depends on the frequency ω. The model used for ε_D depends on the type of metal. It is not restrictive to assume that ε_D is described by a Drude model [28]:

$$\varepsilon_D(\omega) = \varepsilon_0 \left(1 - \frac{\omega_p^2}{\omega\left(\omega + i\tau^{-1}\right)}\right),$$

where ω_p is the plasma frequency of the bulk material and τ is the bulk electron relaxation time. Any similar model can be used [26]. The permeability μ is constant everywhere, $\mu = \mu_m$. We define the wavenumbers $k_D = \omega\sqrt{\varepsilon_D \mu_m}$ and $k_m = \omega\sqrt{\varepsilon_m \mu_m}$. We denote by z_D the centre of the particle D. Up to a translation it is not restrictive to assume that $z_D = 0$. Consider $\Omega \supset D$ a domain of characteristic size $R \gg {k_m}^{-1}$ and $d(D, \partial\Omega) \gg {k_m}^{-1}$. Our goal is to reconstruct $\mathbf{p}^*$ and z^* from the knowledge of far-field data, *i.e.*, the knowledge on $\partial\Omega$ of the field u solving

$$\nabla \cdot \left(\frac{1}{\varepsilon}\nabla u\right) + \omega^2 \mu\, u = \mathbf{p}^* \cdot \nabla \delta_{z^*} \qquad \text{in } \mathbb{R}^2, \tag{1}$$

and satisfying the outgoing Sommerfeld radiation condition

$$\left|\frac{\partial u}{\partial |x|} - i k_m u\right| = \mathcal{O}\left(|x|^{-3/2}\right), \qquad \text{as } |x| \to \infty,$$

uniformly in $x/|x|$, for $\Re k_m > 0$. For simplicity we assume that $\Omega = B_R$ the disk centred at the origin of radius R. The setting is sketched in Figure 1.

Proposition 2.1. *If $\Im \varepsilon_D \neq 0$, then equation (1) is well posed.*

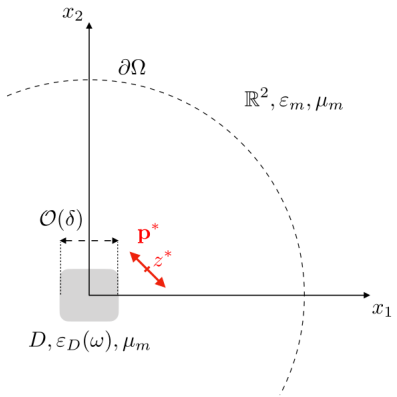

FIGURE 1. Single-point emitter modelled as a dipole of centre z^* and orientation $\mathbf{p}^*$ placed in the vicinity of a plasmonic nanoparticle D centred at the origin.

Proof. This is a classical result. A recent treatment of this exact case can be found in [6]. □

Remark 2.2. The condition $\Im\varepsilon_D \neq 0$ is not sharp, but it is sufficient. The full treatment of the case $\Im\varepsilon_D \to 0$ is done in [25].

2.2. **Relevance of the scalar model.** The scalar Helmholtz equation is the correct way to describe the electromagnetic field propagation in a two-dimensional environment [22, Remark 2.1]. It is relevant to model the propagation of an electromagnetic wave in a medium that is invariant along a coordinate.

Two cases can be modelled. The first one corresponds to the electric field being perpendicular to the propagation plane. It has the form $(0, 0, E_z)$, while the magnetic field has the form $(H_x, H_y, 0)$. This case is referred to as the *transverse electric* case. The other case corresponds to the magnetic field being transverse to the propagation plane. It is called the *transverse magnetic* case. The magnetic field and electric field are $(0, 0, H_z)$ and $(E_x, E_y, 0)$, respectively.

For a non-magnetic medium described by a space-dependant permittivity distribution $\varepsilon(x)$ with $x \in \mathbb{R}^2$ and a constant magnetic permeability, the transverse magnetic case is the most mathematically interesting case, as the spectral properties of the transmission problem for a small obstacle (of characteristic size small compared to the wavelength) are very similar to the ones of the Maxwell transmission problem. Indeed, in the *static regime*, the electric field $\mathbf{E}$ can be written as $\mathbf{E} := \nabla\tilde{u} := (E_x, E_y, 0) := (\nabla u, 0)$. Then the Lippman-Schwinger equation associated with problem (1), *i.e.*, the equation satisfied by the electric field inside the particle $\nabla u = (E_x, E_y)$ is [5]:

$$\eta\nabla u(x) - \nabla \int_D \nabla\Gamma^0(x-y)\cdot\nabla u(y)\mathrm{d}y = \eta D^2 \Gamma^0(x-z^*)\mathbf{p}^*, \qquad x \in D, \tag{2}$$

where Γ^k, $k \geq 0$, is the fundamental outgoing solution to the Helmholtz operator $\Delta + k^2$ given in Appendix A and $\eta = \varepsilon_m/(\varepsilon_m - \varepsilon_D)$ is a contrast parameter that expresses the relative permittivity of the obstacle with respect to the surrounding medium.

In the three-dimensional case, the integral equation satisfied by the electric field $\mathbf{E}$ inside the particle is very similar (see for instance [13] or [5, equation (3.1)])

$$\eta \mathbf{E}(x) - \nabla \int_D \nabla \tilde{\Gamma}^0(x-y) \cdot \mathbf{E}(y) \mathrm{d}y = \eta D^2 \tilde{\Gamma}^0(x-z^*)\mathbf{p}^*, \qquad x \in D, \tag{3}$$

where $\tilde{\Gamma}^k$ is the fundamental solution of the Helmholtz equation in three dimensions.

We can notice a strong similarity between equations (2) and (3), and therefore the scalar model is a good starting point. The full static and low frequency spectral analysis of equation (3) is performed in [10], while the Maxwell case can be found in [7]. In this paper we only focus on the two-dimensional case.

2.3. **Limits of the model.** The mathematical results presented here hold when the size of the nanoparticle becomes very small compared to the wavelength or when the dipole source gets very close to the particle. Nevertheless, the model used to describe the interaction between the fluorescent molecule and the nanoparticle is incorrect when the different scales in the problem become too small, and fails to properly describe the physics of the problem, especially any quantum effect that may appear. We can mention the *quenching* phenomenon that occurs when the molecule gets very close to the nanoparticle (a few nanometers) [12, 14]. When the nanoparticle becomes very small (of characteristic size less than 10nm), the size of the fluorescent molecule can become comparable to the size of the nanoparticle itself. Therefore it is not justified to model the fluorescent molecule as a point dipole, and a more sophisticated (quantum) model has to be considered [24]. However, as mentioned in subsection 1.2, the novelty of the method proposed here is that it can be applied to *larger* nanoparticles, of size smaller but comparable to the wavelength of the electromagnetic field emitted by the fluorescent molecule.

3. Modal approximation of the solution.

In the following section, we recall the results from [10] that are needed for the localisation procedure.

We will use standard *layer potentials* notations. The definitions and symmetrisation process of the Neumann-Poincaré operator on which the theorem relies are recalled in appendix A. We also refer to the book [4] and references therein.

Definition 3.1. We define the *modes* of the system by

$$e_n^\omega(x) := \mathcal{S}_D^{k_m}\left[\varphi_n\right](x), \qquad x \in \mathbb{R}^2 \setminus \overline{D},\ n \in \mathbb{N}^*.$$

$\mathcal{S}_D^{k_m}$ is the single-layer potential and φ_n are the eigenvectors of the Neumann-Poincaré operator $\mathcal{K}_D^*$.

Theorem 3.2. *The unique solution u of (1) can be written as:*

$$u(x) = \nabla \Gamma^{k_m}(x, z^*) \cdot \mathbf{p}^* + \sum_{n=1}^{N} \alpha_n e_n^\omega(x) + \mathcal{E}_N(x), \qquad x \in \mathbb{R}^2 \setminus \overline{D}, N \in \mathbb{N}^*,$$

where α_n are coupling coefficients between the dipole source and the modes that depend on z^*, $\mathbf{p}^*$ and ω. $\mathcal{E}_N(x)$ is an error term that depends on the position of the source, the shape of the particle D, the number of modes considered, and the observation position x. The coupling coefficients α_n have a (rather lengthy) explicit formula that is given in the proof.

Proof. The theorem was proved in [10, proposition 5]. We recall here for the sake of completeness the expression of the coupling coefficients. Define F as

$$F = -\frac{1}{\varepsilon_m}\boldsymbol{\nu}(x)^\top \mathrm{D}^2\Gamma^{k_m}(x,z^*)\mathbf{p}^* - \frac{1}{\varepsilon_D}\left(\frac{1}{2}I - \mathcal{K}_D^{k_D,*}\right)\left(\mathcal{S}_D^{k_D}\right)^{-1}\left[\nabla\Gamma^{k_m}(x,z^*)\cdot\mathbf{p}^*\right],$$

for $x \in \partial D$ and where $\boldsymbol{\nu}(x)$ is the normal vector on ∂D. We denote by λ_n the eigenvalues of the Neumann-Poincaré operator on D (see Appendix A) and introduce the contrast parameter:

$$\lambda(\omega) := \frac{\varepsilon_m + \varepsilon_D(\omega)}{2\left(\varepsilon_m - \varepsilon_D(\omega)\right)},$$

as well as

$$\tau_n(\omega) = \left(\frac{1}{\varepsilon_D} - \frac{1}{\varepsilon_m}\right)\left(\lambda(\omega) - \lambda_n\right) + \left(\omega\delta c^{-1}\right)^2 \log\left(\omega\delta c^{-1}\right)\tau_{n,1},$$

where $\tau_{n,1}$ is a perturbative spectral parameter defined in definition A.2. Then [10, proposition 5] gives us the following expansion for u:

$$u(x) = \nabla\Gamma^{k_m}(x,z^*)\cdot\mathbf{p}^* + \sum_{n=1}^{N}\frac{\langle F,\varphi_n\rangle_{\mathcal{H}^*}}{\tau_n(\omega)}\mathcal{S}_D^{k_m}\left[\varphi_n\right](x) + \mathcal{E}_N(x), \qquad x \in \mathbb{R}^2 \setminus \overline{D}.$$

for $N \in \mathbb{N}^*$. By setting $\alpha_n := \langle F,\varphi_n\rangle_{\mathcal{H}^*}/(\tau_n(\omega))$ we get the result. □

Remark 3.3. The coupling coefficients

$$\alpha_n = \frac{\langle F,\varphi_n\rangle_{\mathcal{H}^*}}{\tau_n(\omega)}$$

can become very large if $\tau_n(\omega) \ll 1$. This will occur if ω approaches a plasmonic resonance frequency. In the case that $\langle F,\varphi_n\rangle_{\mathcal{H}^*} \neq 0$ and $\tau_n(\omega) \ll 1$, the field scattered by the nanoparticle may become very large and contribute to the far field as much as the radiating dipole, making it very challenging to localise the dipole, as the imaging system will be *blinded* by the nanoparticle.

Remark 3.4. The number of modes that have to be considered to obtain a good approximation of the field is a complicated question because the modal approximation is not uniform, neither with respect to the observation point x, nor with the frequency ω or the source parameters $(\mathbf{p}^*, z^*)$. However, in practice, only a few modes are needed to correctly describe the scattered field. In three dimensions, this is due to the fact that:

1. the *coupling coefficient* of the mode n to the source
$$\alpha_n = \frac{\langle F,\varphi_n\rangle_{\mathcal{H}^*}}{\tau_n(\omega)}$$
have super-polynomial decay with respect to n for a fixed source and frequency [10, proposition 3],
2. high-order modes do not contribute to the far field. It has been shown in [9] that, in the static case ($\omega = 0$), the contribution of the modes outside the particle decay exponentially with the order of the mode. It has not been demonstrated in the dynamic case $\omega \neq 0$ but there are numerical indications that the result probably holds for $\omega \neq 0$.

So even though it is difficult to obtain a quantitative estimate of the error term in Theorem 3.2, in practical situations the finite sum on the right-hand side of the solution makes for a good approximation.

4. **Localisation.** We now introduce a method that recovers a dipole source's position and orientation in the presence of a resonant nanoparticle at a low computational cost. It is based on the modification of a back-propagation/holography procedure, but the principle of the method works with any linear imaging functional.

In the absence of a resonant structure, super-localisation is possible through the modelling of a *point spread function* (PSF) of the imaging system, that maps a single point-like source to an image. Then the location of the point source is obtained by finding the centre of the PSF, which can be done with a precision that depends only on the signal-to-noise ratio. In general, it is achieved with a least-square procedure, i.e. by fitting the centre of the PSF on the image.

In the presence of the resonant structure, the image will not be the PSF, but the superposition of the PSF at the location of the dipole with the image of the nanoparticle. The current state-of-the-art method to recover the correct position of an emitter near a nanoparticle requires solving the forward problem (the full-wave Maxwell equations) for each position of the source [16]. This is very costly in terms of computation, making it impossible to apply in practical situations where thousands of isolated single emitters have to be localised quickly.

The idea behind our method is that even though the field scattered by the nanoparticle cannot be known in advance (as it depends on both the position and the orientation of the dipole), it can be expressed as a linear combination of pre-computable quantities (the modes). This suggests that the distortion of the PSF due to the presence of the nanoparticle is simply a linear combination of pre-computable artefacts. Therefore, instead of performing the least-square procedure on the position of the centre of the PSF, we optimise on both the centre of the PSF and the coefficients of the linear combination of artefacts.

4.1. **Back-propagation in the absence of a resonant structure.** Super-localisation of the fluorescent molecule is obtained by back-propagating $u(x)$, for $|x|$ large enough, and maximising the back-propagation function. The precision of the localisation is limited by the signal-to-noise ratio (SNR).

We introduce the following vector-valued imaging functional.

Definition 4.1.

$$\mathcal{I}(z) = \int_{\partial B_R} \overline{\nabla_z \Gamma^{k_m}(x,z)} u(x) \mathrm{d}\sigma(x), \quad z \in \Omega,$$

where the imaging domain Ω is such that

$$D \Subset \Omega \Subset B_R.$$

We then include a lemma from [3] with its proof for sake of completeness.

Lemma 4.2. *Let*

$$\mathcal{R}(y,z) = \int_{\partial B_R} \overline{\nabla_y \Gamma^{k_m}(x,y)} \nabla_z \Gamma^{k_m}(x,z)^\top \mathrm{d}\sigma(x), \qquad (y,z) \in \mathbb{R}^4.$$

Then

$$\lim_{R\to\infty} \mathcal{R}(z,z) = \frac{k_m}{8} I_2,$$

where I_2 is the identity matrix.

Proof. We start from the Helmholtz-Kirchhoff theorem [2]

$$\lim_{R\to\infty} \mathcal{R}(y,z) = -\frac{1}{k_m}\nabla_y\nabla_z\Im\,\Gamma^{k_m}(y,z),$$

where $\Im$ is the imaginary part. We can then compute an approximation of $\mathcal{R}$:

$$\frac{1}{k_m}\nabla_y\nabla_z\Im\,\Gamma^{k_m}(y,z) = \frac{1}{4}\Bigg[k_m J_0\left(k_m|y-z|\right)\frac{(y-z)\,(y-z)^\top}{|y-z|^2} - 2\frac{J_1\left(k_m|y-z|\right)}{|y-z|}\frac{(y-z)\,(y-z)^\top}{|y-z|^2} + \frac{J_1\left(k_m|y-z|\right)}{|y-z|}I_2\Bigg].$$

One can see that $\mathcal{R}(y,z)$ decays as $|y-z|^{-1/2}$ and the imaging functional has a peak at $y=z$. Evaluating at $y=z$ gives the result. □

It is easy to see from lemma 4.2 that in the absence of the resonant structure, $\mathcal{I}(z)$ would have an amplitude peak at $z=z^*$ and that its orientation would be parallel to $\mathbf{p}^*$. To get z^* and $\mathbf{p}^*$ one needs to solve the following optimisation problem in $\mathbb{R}^4$:

$$(z^*,\mathbf{p}^*) = \underset{z,\mathbf{p}}{\operatorname{argmin}} \left\|\mathcal{I}(\cdot) - \mathcal{R}(\cdot,z)\mathbf{p}\right\|_{L^2(\Omega)}. \tag{4}$$

4.2. **Back-propagation in the presence of the resonant structure.**

Proposition 4.3. *In the presence of the nanoparticle, the imaging functional has the form:*

$$\mathcal{I}(z) = \mathcal{R}(z,z^*)\mathbf{p}^* + \sum_{n=1}^{N}\alpha_n I_{e_n}(z) + I_{\mathcal{E}_N}(z),$$

where α_n are the (unknown) coupling coefficients defined in Theorem 3.2, I_{e_n} the (known) image by the imaging functional of the mode n and $I_{\mathcal{E}_n}(z)$ the (unknown) image of the error term.

Proof. The result is a direct consequence of Theorem 3.2 and the linearity of the imaging functional. Let

$$I_{e_n}(z) = \int_{\partial B_R} \overline{\nabla_z\Gamma^{k_m}(x,z)}e_n(x)\mathrm{d}\sigma(x),$$

and

$$I_{\mathcal{E}_N}(z) = \int_{\partial B_R} \overline{\nabla_z\Gamma^{k_m}(x,z)}\mathcal{E}_N(x)\mathrm{d}\sigma(x).$$

We obtain the result by applying lemma 4.2. □

To recover z^* and $\mathbf{p}^*$ in the presence of the resonant structure, we now solve an optimisation problem in $\mathbb{R}^{4+2N}$:

$$\left(z^*,\mathbf{p}^*,(\beta_n^*,\gamma_n^*)_{n=1}^N\right) = \underset{z,\mathbf{p},(\beta_n,\gamma_n)_{n=1}^N}{\operatorname{argmin}} \left\|\mathcal{I}(\cdot) - \mathcal{R}(\cdot,z)\mathbf{p} - \sum_{n=1}^{N}(\beta_n+i\gamma_n)I_{e_n}(z)\right\|^2_{L^2(\Omega)}, \tag{5}$$

where β_n and γ_n are the real and imaginary part of α_n, respectively.

5. **Numerical simulations.** In this section we illustrate the method's efficiency with numerical simulations. We perform a virtual experiment where a dipole source is placed near a metallic nanoparticle whose permittivity is described by a Drude model. We consider nanoparticles with various shapes and subject to noise to illustrate the robustness of the method.

5.1. **Geometry and physical parameters.** Throughout this section, we consider the three domains sketched on Figure 2. The five-petal flower (a) is defined by $\varrho = \delta(2 + 0.6\cos(5\theta))$ in polar coordinates. The rounded diamond (b) is defined by the parametric curve $\zeta(\theta) = 2\delta\left(e^{i\theta} + 0.066e^{-3i\theta}\right)$, for $\theta \in [0, 2\pi]$. The narrow ellipse (c) semi-axes are on the x_1- and x_2- axes and are of length $a = 1\delta$ and $b = 5\delta$, respectively.

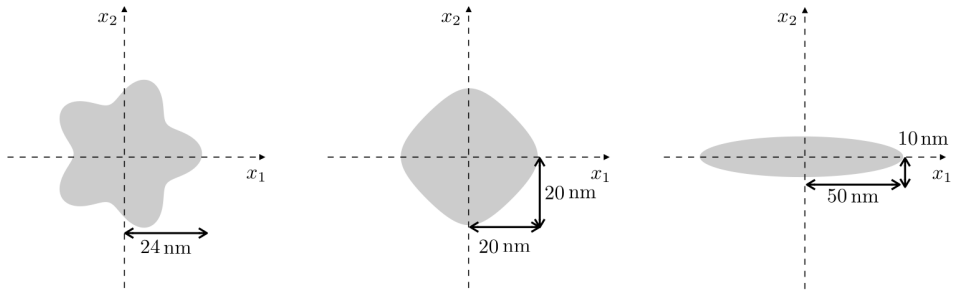

FIGURE 2. Sketch of the three reference domains: the five-petal flower (a), the rounded diamond (b) and the narrow ellipse (c).

We recall that the permittivity inside the particle is described by a Drude model and that the homogeneous medium is taken to be vacuum:

$$\varepsilon_D(\omega) = \varepsilon_0 \left(1 - \frac{\omega_p^2}{\omega\left(\omega + i\tau^{-1}\right)}\right).$$

The physical parameters are chosen as $\omega_p = 2 \cdot 10^{15}$ Hz, $T = 10^{-14}$s, $\varepsilon_0 = 8.854187128 \cdot 10^{-12}$ Fm^{-1}, $\mu_0 = 4\pi \cdot 10^{-7}$ Hm^{-1} and $\delta = 10^{-8}$ m.

5.2. **Modes and resonances.** For a given domain, we compute a list of N plasmonic resonant frequencies $(\omega_n)_{n\in[1,N]}$, as well as their associated modes. We illustrate the fist six modes of the rounded diamond in Figure 3.

5.3. **Imaging experiment.** For a given domain, we pick a resonant frequency ω_n and place an oscillating dipole at frequency ω_n near the nanoparticle. We choose the frequency that corresponds to a mode that has a dipole radiation pattern, in order to maximise the effect of the nanoparticle's presence on the far-field image and make the localisation of the dipole source as hard as possible.

The scattered field (solution of (1)) is then computed by solving a system of boundary integral equations (that involves layer potential techniques) detailed in appendix A. The boundary of the nanoparticle is discretised using 2^8 points.

The field (both its amplitude and phase) is measured in the far field on a disk of radius 3000δ and back-propagated using the imaging functional introduced in definition 4.1.

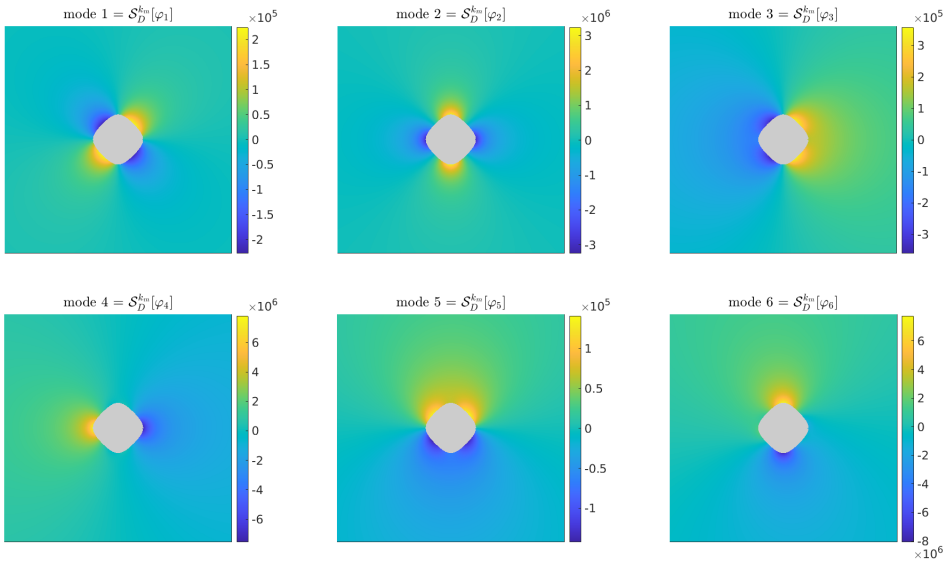

FIGURE 3. First 6 modes for the rounded diamond, corresponding to $\omega = 1.5050 \cdot 10^{15}$ Hz.

5.4. **Localisation by optimisation and mirage.** The localisation (without correction) of the particle is achieved by fitting a focal spot on the imaging functional, as described in equation (4). The optimisation is done using the *fmincon* MATLAB® function. We constrain the search to a $300 \times 300\text{nm}^2$ square. The position of the initial guess does not influence the result.

For the corrected functional, we use the *fmincon* function to search for a solution of equation (5). The number of modes to use for the correction will be discussed later in this section.

We show, on Figure 4, examples of the results of the optimisation procedure for the three different domains. The dipole position is represented as a star and its orientation is shown in the inset. The results of the optimisation procedures are shown for the corrected and uncorrected functionals, as crosses and circles, respectively. This illustrates the mirage effect and the efficiency of the correction technique with three different scenarios. In the following sections we go into more details. We study the sensitivity on the distance and number of modes and the stability with respect to measure noise.

5.5. **Sensitivity analysis.** On Figure 5 we plot the error on the localisation (a) and orientation (b) of the dipole with respect to the distance between the emitter and the nanoparticle. We initially place the dipole at $z^* = [18.65, 16.65]$nm and fix its orientation ($\mathbf{p}^* = (-1, 1)$). We gradually increase the distance to the nanoparticle by translating the dipole along a radial component of a disk centred at the origin. As expected, the uncorrected functional does not behave well when the source is close to the nanoparticle. Note that the error is still one order of magnitude below the usual diffraction limit. The localisation error on the corrected functional is one order of magnitude lower than the uncorrected one. The correction achieves a major improvement when the emitter is close enough to excite the nanoparticle. When

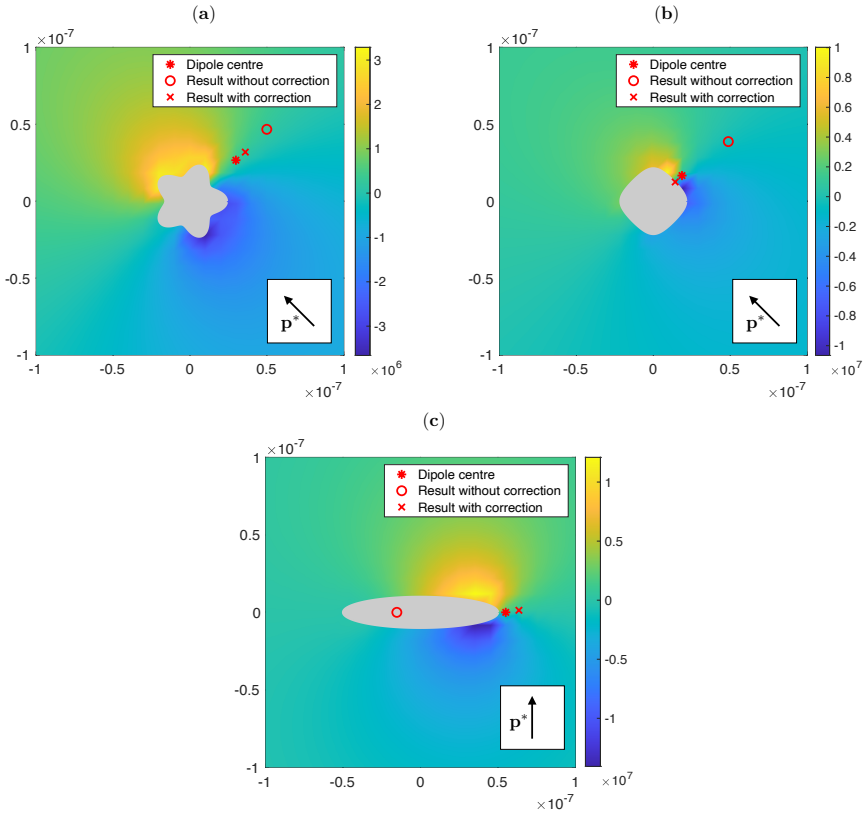

FIGURE 4. Mirage and optimisation on the three domains: for the flower (a), the localisation error is 29nm before correction and 8nm after. For the diamond (b), the error is 37nm before correction and 5.6nm after. The dipole direction is $(-1, 1)$. For the ellipse (c), the localisation error is 71nm before correction and 8nm after and the dipole direction is $(0, 1)$.

the emitter is far away and the coupling is weaker, both procedures have similar performances.

5.6. **Stability with respect to measurement noise.** We compute the imaging functional with a set of data perturbed by Gaussian white noise. We consider the case in which the measured field $u(x)$ is corrupted by an additive noise $\nu(x)$, $x \in \partial B_R$. We assume that ∂B_R is covered uniformly with sensors and that the additive noises $\nu(x)$ have independant and identically distributed $\mathcal{N}(0, \sigma_{\text{noise}})$ entries. Hence, the entries of $\nu(x)$ are independant Gaussian random variables with mean zero and variance

$$\sigma_{\text{noise}} = \sigma_0 \|u\|_F / \sqrt{N},$$

where $||\ ||_F$ is the Frobenius norm, σ_0 the noise percentage and N the number of sensors.

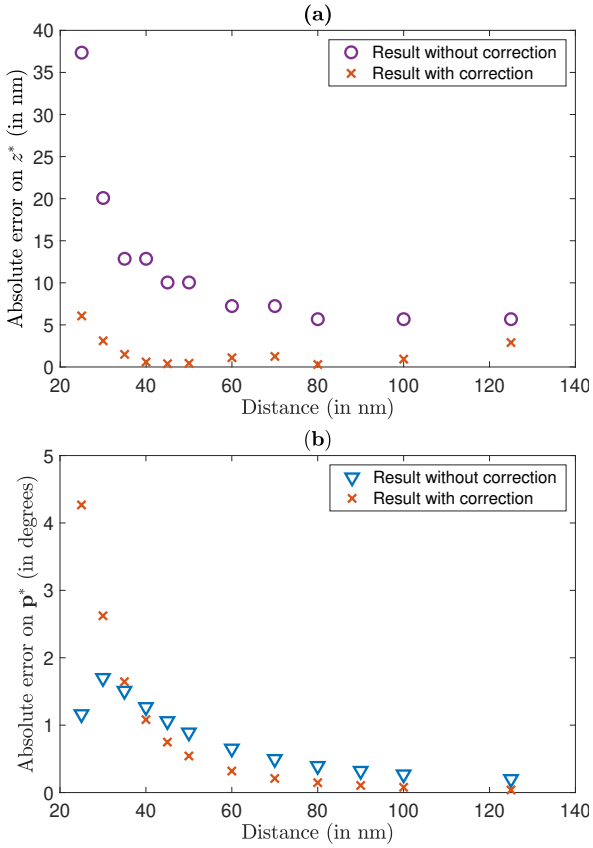

FIGURE 5. (a) Absolute error on the position z^* in nanometers with (orange crosses) and without (purple circles) correction against the distance between the emitter and the rounded diamond boundary. (b) Absolute error on the orientation $\mathbf{p}^*$ in degrees with (orange crosses) and without (blue triangles) correction against the distance between the emitter and the rounded diamond boundary. The initial position is $z^* = [18.65, 16.65]$nm. The dipole direction is $(-1, 1)$.

For each noise level, we average the results over 100 realisations. Figure 6 presents the results of computational experiments in the case in which the nanoparticle is the diamond. It shows that the corrected imaging functional performs well at high levels of noise, which means that the corrected imaging functional is robust with respect to additive measurement noise.

5.7. **Number of modes.** For the numerical experiments of this section we have assumed to know in advance the pre-computable artefacts that describe the distortion of the PSF due to the presence of the nanoparticle, *i.e.*, the modes excited by the fluorescent molecule. In practice, this may not be the case. However, we know that only a few modes are excited and contribute significantly to approximate the scattered field. One can ask whether optimising over excited *and* unexcited modes

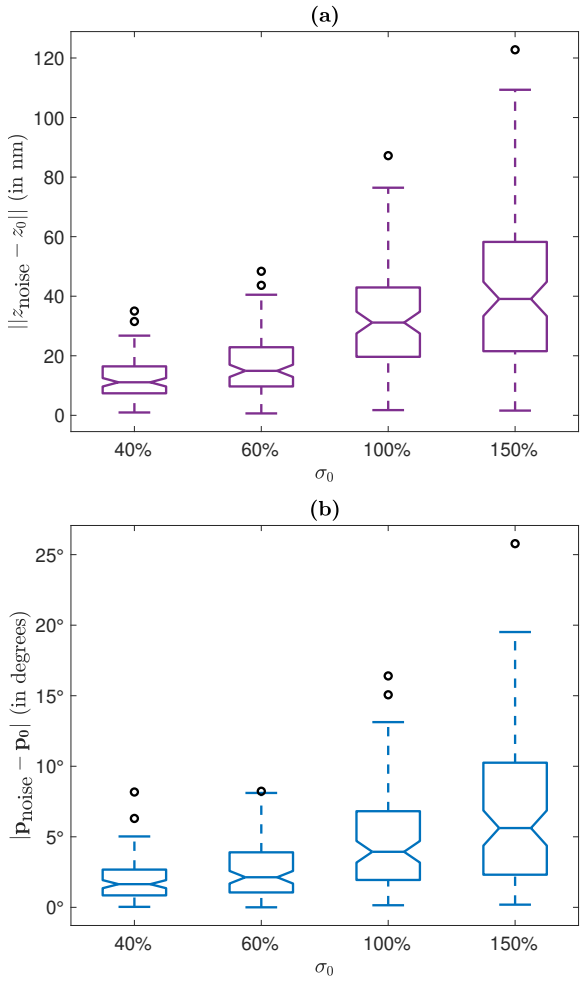

FIGURE 6. Boxplots showing the error on the position (a) and orientation (p) for noise levels σ_0 varying from 40% to 150%. The boxplots show the median, 25- and 75-quartiles, the notches correspond to the 95 confidence interval for 100 realisations. The outliers are shown as black symbols.

will give results as good as the ones obtained by optimising over the excited modes only.

For these simulations we consider the rounded diamond. The dipole position is $[18.65, 16.65]$nm. The initial direction is $(-1, 1)$. In this case, we can check numerically that only modes 4 and 6 suffice to approximate the field.

On Table 1, we show the error on the position and orientation for the first N modes. As expected, the error becomes small as soon as $N \geq 6$, *i.e.*, modes 4 and 6 are considered, regardless of the number of unexcited modes used for the optimisation procedure.

N modes	2	3	4	5	6	7
$\|\|\mathbf{p_N} - \mathbf{p}^*\|\|$ (in deg)	0.57	89.2	13.9	45.0	0.57	0.30
$\|\|z_N - z^*\|\|$ (in nm)	116	145	116	166	4.74	4.22

TABLE 1. Error on the position and orientation when accounting only for the first N modes, $N = 2..7$.

6. **Concluding remarks.** In this paper we propose a new method that precisely recovers the localisation of a single isolated source placed in a resonant environment at a low computational cost. Using the recent results of [10, 7] and pre-computing the modes of the resonant structure, we transform the *inverse source problem for the wave equation* into a simple minimisation algorithm in $\mathbb{R}^d$ with d being the number of modes to consider, usually less than 10. We are able to recover the position of the source with a precision that is two orders of magnitude below the usual diffraction limit. Since most of the computational cost comes from the pre-computation of the modes, the position of many single sources can be recovered very quickly, which corresponds to the needs of real *PALM* or *STORM* experiments, where the position of thousands of emitters are necessary to produce an image. This article acts like a proof of concept for our method. In a forthcoming paper, we will adapt the numerics for the three-dimensional Maxwell case that is better suited for applications, and consider a more complex structured environment as well as amplitude only measurements.

Appendix A. **Layer potentials.** The results presented in this section are all classical and can be found in the books [4, 2].

A.1. **Operator.** For $k \geq 0$, a fundamental solution to the Helmholtz operator $\Delta + k^2$ is given by

$$\Gamma^k(x) = \begin{cases} \dfrac{1}{2\pi} \ln|x| & \text{if } k = 0, \\ -\dfrac{i}{4} H_0^{(1)}(k|x|) & \text{if } k > 0, \end{cases}$$

for $x \neq 0$, where $H_0^{(1)}$ is the well-known Hankel function of the first kind and order zero. Let $\mathcal{S}_D^k$ be the single layer potential, defined by

$$\mathcal{S}_D^k[\phi](x) = \int_{\partial D} \Gamma^k(x,y)\phi(y)\mathrm{d}\sigma(y), \qquad x \in \mathbb{R}^2, \tag{6}$$

for $\phi \in L^2(\partial D)$. We also define the Neumann-Poincaré operator by

$$\mathcal{K}_D^{k,*}[\phi](x) = \int_{\partial D} \frac{\partial \Gamma^k(x,y)}{\partial \nu(x)} \phi(y)\mathrm{d}\sigma(y), \qquad x \in \partial D, \tag{7}$$

for $\phi \in L^2(\partial D)$, where $\partial/\partial\nu(x)$ denotes the outward normal derivative at $x \in \partial D$. When $k = 0$, we omit the superscript and write $\mathcal{S}_D$ and $\mathcal{K}_D^*$ for simplicity. Let $\langle \cdot, \cdot \rangle_{-1/2,1/2}$ be the duality pairing between $H^{-\frac{1}{2}}(\partial D)$ and $H^{\frac{1}{2}}(\partial D)$, where $H^{\frac{1}{2}}(\partial D)$ is the Sobolev space of order $1/2$. The single layer potential is, in general, not invertible in $L^2(\partial D)$. Let us introduce

$$\widetilde{\mathcal{S}}_D[v] = \begin{cases} \mathcal{S}_D[v] & \text{if } \langle v, \chi(\partial D)\rangle_{-\frac{1}{2},\frac{1}{2}} = 0, \\ -\chi(\partial D) & \text{if } v = \varphi_0, \end{cases}$$

with φ_0 being the unique (in the case of a single particle) eigenfunction of $\mathcal{K}_D^*$ associated with eigenvalue $1/2$ such that $\langle \varphi_0, \chi(\partial D)\rangle_{-\frac{1}{2},\frac{1}{2}} = 1$. The operator $\mathcal{K}_D^* : H^{-1/2}(\partial D) \to H^{-1/2}(\partial D)$ is compact and the following Plemelj's symmetrisation principle identity (also known as Calderón) holds on $H^{-1/2}(\partial D)$:

$$\widetilde{\mathcal{S}}_D \mathcal{K}_D^* = \mathcal{K}_D \widetilde{\mathcal{S}}_D.$$

Let $\mathcal{H}^*(\partial D)$ be the space $H^{-1/2}(\partial D)$ equipped with the following inner product:

$$\langle u, v\rangle_{\mathcal{H}^*(\partial D)} = -\left\langle \widetilde{\mathcal{S}}_D[v], u \right\rangle_{-1/2,1/2}.$$

The Neumann-Poincaré operator $\mathcal{K}_D^*$ is self-adjoint in the Hilbert space $\mathcal{H}^*(\partial D)$. Let $(\lambda_n, \varphi_n)_{n\in\mathbb{N}}$ be the eigenvalue and normalised eigenfunction pair of $\mathcal{K}_D^*$ in $\mathcal{H}^*(\partial D)$. Then $\lambda_0 = 1/2$, $-1/2 < \lambda_n < 1/2$ for $n \geq 1$ and $\lambda_n \to 0$ as $n \to +\infty$.

A.2. **Solution for the wave equation.** Let $H^{1/2}(\partial D)$ be the usual Sobolev space and let $H^{-1/2}(\partial D)$ be its dual space with respect to the duality pairing $\langle \cdot, \cdot \rangle_{-\frac{1}{2},\frac{1}{2}}$. The field u can be represented using the single-layer potentials $\mathcal{S}_D^{k_c}$ and $\mathcal{S}_D^{k_m}$, introduced in equation (6), as follows:

$$u(x) = \begin{cases} \mathcal{S}_D^{k_c}[\Phi](x), & x \in D, \\ u^{\text{in}}(x) + \mathcal{S}_D^{k_m}[\Psi](x), & x \in \mathbb{R}^d \setminus \overline{D}, \end{cases} \tag{8}$$

where the pair $(\Phi, \Psi) \in H^{-\frac{1}{2}}(\partial D) \times H^{-\frac{1}{2}}(\partial D)$ is the unique solution to

$$\begin{cases} \mathcal{S}_D^{k_m}[\Psi](x) - \mathcal{S}_D^{k_c}[\Phi](x) = F_1, & x \in \partial D, \\ \dfrac{1}{\varepsilon_m}\left(\dfrac{1}{2}I + \mathcal{K}_D^{k_m,*}\right)[\Psi](x) + \dfrac{1}{\varepsilon_c}\left(\dfrac{1}{2}I - \mathcal{K}_D^{k_c,*}\right)[\Phi](x) = F_2, & x \in \partial D, \end{cases} \tag{9}$$

and

$$F_1 = -u^{\text{in}}(x), \qquad F_2 = -\frac{1}{\varepsilon_m}\frac{\partial u^{\text{in}}(x)}{\partial \nu}, \qquad x \in \partial D,$$

where $\mathcal{K}_D^{k_m,*}$ is the Neumann-Poincaré operator introduced in equation (7) and $u^{\text{in}} = \mathbf{p}^* \cdot \nabla \Gamma^k(\cdot, z^*)$.

A.3. **Definition of $\tau_{n,1}$.**

Lemma A.1. *For k small enough, the two-dimensional boundary operator $\widehat{\mathcal{S}}_D^k : \mathcal{H}^*(\partial D) \to \mathcal{H}^*(\partial D)$ defined as*

$$\widehat{\mathcal{S}}_D^k[\phi](x) = \mathcal{S}_D^0[\phi](x) + \eta_k \int_{\partial D} \phi(y) \mathrm{d}\sigma(y), \tag{10}$$

is invertible and

$$\left(\widehat{\mathcal{S}}_D^k\right)^{-1} = \widetilde{\mathcal{S}}_D^{-1} - \left\langle \widetilde{\mathcal{S}}_D^{-1}[\cdot], \varphi_0 \right\rangle_{\mathcal{H}^*(\partial D)} \varphi_0 - \mathcal{U}_k, \tag{11}$$

where

$$\mathcal{U}_k = \frac{\left\langle \widetilde{\mathcal{S}}_D^{-1}[\cdot], \varphi_0 \right\rangle_{\mathcal{H}^*(\partial D)}}{\mathcal{S}_D[\varphi_0] + \eta_k} \varphi_0$$

and $\eta_k = (1/2\pi)(\log k + \gamma - \log 2) - i/4$, with the constant γ being the Euler constant. Note that $\mathcal{U}_k = \mathcal{O}(1/\log k)$.

Definition A.2.

$$\tau_{n,1} = \langle \mathcal{A}_{D,1}\varphi_n, \varphi_n \rangle_{\mathcal{H}^*(\partial D)}$$

with

$$\mathcal{A}_{D,1} = \frac{1}{\varepsilon_m}\mathcal{K}_{D,1}^{(1)}(I - \mathcal{P}_{\mathcal{H}_0^*}) + \left(\frac{1}{2}I - \mathcal{K}_D^*\right)\widetilde{\mathcal{S}}_D^{-1}\mathcal{S}_{D,1}^{(1)}\left(\frac{1}{\varepsilon_D}I - \frac{1}{\varepsilon_m}\mathcal{P}_{\mathcal{H}_0^*}\right),$$

Acknowledgments. The authors thank Habib Ammari for helpful conversations.

REFERENCES

[1] H. Ammari, Y. Deng and P. Millien, Surface plasmon resonance of nanoparticles and applications in imaging, *Archive for Rational Mechanics and Analysis*, **220** (2016), 109-153.

[2] H. Ammari, J. Garnier, W. Jing, H. Kang, M. Lim, K. Sølna and H. Wang, *Mathematical and Statistical Methods for Multistatic Imaging*, vol. 2098, Springer, 2013.

[3] H. Ammari, J. Garnier and P. Millien, Backpropagation imaging in nonlinear harmonic holography in the presence of measurement and medium noises, *SIAM Journal on Imaging Sciences*, **7** (2014), 239-276.

[4] H. Ammari, H. Kang and H. Lee, *Layer Potential Techniques in Spectral Analysis*, vol. 153 of Mathematical Surveys and Monographs, American Mathematical Society, Providence, 2009.

[5] H. Ammari and P. Millien, Shape and size dependence of dipolar plasmonic resonance of nanoparticles, *Journal de Mathématiques Pures et Appliquées*, **129** (2019), 242-265.

[6] H. Ammari, P. Millien, M. Ruiz and H. Zhang, Mathematical analysis of plasmonic nanoparticles: The scalar case, *Arch. Ration. Mech. Anal.*, **224** (2017), 597-658.

[7] H. Ammari, P. Millien and A. L. Vanel, Modal approximation for strictly convex plasmonic resonators in the time domain: The Maxwell's equations, *Journal of Differential Equations*, **309** (2022), 676-703.

[8] K. Ando and H. Kang, Analysis of plasmon resonance on smooth domains using spectral properties of the Neumann-Poincaré operator, *Journal of Mathematical Analysis and Applications*, **435** (2016), 162-178.

[9] K. Ando, H. Kang, Y. Miyanishi and T. Nakazawa, Surface localization of plasmons in three dimensions and convexity, *SIAM Journal on Applied Mathematics*, **81** (2021), 1020-1033.

[10] L. Baldassari, P. Millien and A. L. Vanel, Modal approximation for plasmonic resonators in the time domain: The scalar case, *Partial Differential Equations and Applications*, **2** (2021), Paper No. 46, 40 pp.

[11] D. Bouchet, J. Scholler, G. Blanquer, Y. De Wilde, I. Izeddin and V. Krachmalnicoff, Probing near-field light–matter interactions with single-molecule lifetime imaging, *Optica*, **6** (2019), 135-138.

[12] E. Castanié, M. Boffety and R. Carminati, Fluorescence quenching by a metal nanoparticle in the extreme near-field regime, *Optics Letters*, **35** (2010), 291-293.

[13] M. Costabel, E. Darrigrand and H. Sakly, The essential spectrum of the volume integral operator in electromagnetic scattering by a homogeneous body, *Comptes Rendus Mathematique*, **350** (2012), 193-197.

[14] A. Delga, J. Feist, J. Bravo-Abad and F. Garcia-Vidal, Quantum emitters near a metal nanoparticle: Strong coupling and quenching, *Physical Review Letters*, **112** (2014), 253601.

[15] M. Ehrenberg, The nobel prize in chemistry 2014 (press release), 2014, URL `https://www.nobelprize.org/prizes/chemistry/2014/press-release/`.

[16] B. Fu, B. P. Isaacoff and J. S. Biteen, Super-resolving the actual position of single fluorescent molecules coupled to a plasmonic nanoantenna, *ACS Nano*, **11** (2017), 8978-8987.

[17] M. W. Gramlich, J. Bae, R. C. Hayward and J. L. Ross, Fluorescence imaging of nanoscale domains in polymer blends using stochastic optical reconstruction microscopy (storm), *Optics Express*, **22** (2014), 8438-8450.

[18] D. Grieser, The plasmonic eigenvalue problem, *Reviews in Mathematical Physics*, **26** (2014), 1450005.

[19] S. W. Hell, S. J. Sahl, M. Bates, X. Zhuang, R. Heintzmann, M. J. Booth, J. Bewersdorf, G. Shtengel, H. Hess, P. Tinnefeld, et al., The 2015 super-resolution microscopy roadmap, *Journal of Physics D: Applied Physics*, **48** (2015), 443001.

[20] B. Huang, M. Bates and X. Zhuang, Super-resolution fluorescence microscopy, *Annual Review of Biochemistry*, **78** (2009), 993-1016.

[21] K. L. Kelly, E. Coronado, L. L. Zhao and G. C. Schatz, The optical properties of metal nanoparticles: The influence of size, shape, and dielectric environment, ChemInform, **34** (2003).
[22] A. Moiola and E. A. Spence, Acoustic transmission problems: Wavenumber-explicit bounds and resonance-free regions, *Mathematical Models and Methods in Applied Sciences*, **29** (2019), 317-354.
[23] A. Moroz, Depolarization field of spheroidal particles, *JOSA B*, **26** (2009), 517-527.
[24] T. Neuman, R. Esteban, D. Casanova, F. J. García-Vidal and J. Aizpurua, Coupling of molecular emitters and plasmonic cavities beyond the point-dipole approximation, *Nano Letters*, **18** (2018), 2358-2364.
[25] H.-M. Nguyen, Limiting absorption principle and well-posedness for the Helmholtz equation with sign changing coefficients, *Journal de Mathématiques Pures et Appliquées*, **106** (2016), 342-374.
[26] M. A. Ordal, L. L. Long, R. J. Bell, S. E. Bell, R. R. Bell, R. W. Alexander and C. A. Ward, Optical properties of the metals al, co, cu, au, fe, pb, ni, pd, pt, ag, ti, and w in the infrared and far infrared, *Applied Optics*, **22** (1983), 1099-1119.
[27] M. Raab, C. Vietz, F. D. Stefani, G. P. Acuna and P. Tinnefeld, Shifting molecular localization by plasmonic coupling in a single-molecule mirage, *Nature Communications*, **8** (2017), 13966.
[28] D. Sarid and W. A. Challener, *Modern Introduction to Surface Plasmons: Theory, Mathematica Modeling, and Applications*, Cambridge University Press, 2010.
[29] B. E. Urban, B. Dong, T.-Q. Nguyen, V. Backman, C. Sun and H. F. Zhang, Subsurface super-resolution imaging of unstained polymer nanostructures, *Scientific Reports*, **6** (2016), 1-9.
[30] K. A. Willets, A. J. Wilson, V. Sundaresan and P. B. Joshi, Super-resolution imaging and plasmonics, *Chemical Reviews*, **117** (2017), 7538-7582.

Received for publication July 2022; early access October 2022.